SLAC-PUB-15385

EUROPEAN ORGANIZATION FOR NUCLEAR RESEARCH

CERN-PH-EP-2012-185
27 June 2012

New measurement of the $K^{\pm} \to \pi^+\pi^- e^{\pm}\nu$ (K_{e4}) decay Branching Ratio and Hadronic Form Factors

The NA48/2 Collaboration [1]

Abstract

A sample of more than one million $K^{\pm} \to \pi^+\pi^- e^{\pm}\nu$ (K_{e4}) decay candidates with less than one percent background contamination has been collected by the NA48/2 experiment at the CERN SPS in 2003–2004, allowing a detailed study of the decay properties. The branching ratio, inclusive of $K_{e4\gamma}$ decays, is measured to be $\mathrm{BR}(K_{e4}) = (4.257 \pm 0.016_{\mathrm{exp}} \pm 0.031_{\mathrm{ext}}) \times 10^{-5}$ with a total relative error of 0.8%. This measurement complements the study of S- and P-wave hadronic form factors by assigning absolute values to the relative hadronic form factors obtained earlier in a simultaneous analysis of the $\pi\pi$ scattering lengths conducted on the same data sample. The overall form factor normalization $f_s = 5.705 \pm 0.017_{\mathrm{exp}} \pm 0.031_{\mathrm{ext}}$ is obtained with a total relative precision of 0.6%.

Submitted for publication in Physics Letters B

[1] contact: spasimir.balev@cern.ch, brigitte.bloch-devaux@cern.ch

Published in arXiv: 1206.7065.

Work supported in part by US Department of Energy contract DE-AC02-76SF00515.

SLAC National Accelerator Laboratory, Menlo Park, CA 94025

The NA48/2 Collaboration

J.R. Batley, G. Kalmus, C. Lazzeroni [1], D.J. Munday, M.W. Slater [1], S.A. Wotton
Cavendish Laboratory, University of Cambridge, Cambridge, CB3 0HE, UK [2]

R. Arcidiacono [3], G. Bocquet, N. Cabibbo [4], A. Ceccucci, D. Cundy [5], V. Falaleev, M. Fidecaro, L. Gatignon, A. Gonidec, W. Kubischta, A. Norton [6], A. Maier, M. Patel [7], A. Peters
CERN, CH-1211 Genève 23, Switzerland

S. Balev [8], P.L. Frabetti, E. Gersabeck [9], E. Goudzovski [1], P. Hristov [8], V. Kekelidze, V. Kozhuharov [10], L. Litov [10], D. Madigozhin, N. Molokanova, I. Polenkevich, Yu. Potrebenikov, S. Stoynev [11], A. Zinchenko
Joint Institute for Nuclear Research, 141980 Dubna, Moscow region, Russia

E. Monnier [12], E. Swallow, R. Winston
The Enrico Fermi Institute, The University of Chicago, Chicago, IL 60126, USA

P. Rubin [13], A. Walker
Department of Physics and Astronomy, University of Edinburgh, JCMB King's Buildings, Mayfield Road, Edinburgh, EH9 3JZ, UK

W. Baldini, A. Cotta Ramusino, P. Dalpiaz, C. Damiani, M. Fiorini [14], A. Gianoli, M. Martini, F. Petrucci, M. Savrié, M. Scarpa, H. Wahl
Dipartimento di Fisica dell'Università e Sezione dell'INFN di Ferrara, I-44100 Ferrara, Italy

A. Bizzeti [15], M. Lenti, M. Veltri [16]
Sezione dell'INFN di Firenze, I-50125 Firenze, Italy

M. Calvetti, E. Iacopini, G. Ruggiero [8]
Dipartimento di Fisica dell'Università e Sezione dell'INFN di Firenze, I-50125 Firenze, Italy

M. Behler, K. Eppard, K. Kleinknecht, P. Marouelli, L. Masetti, U. Moosbrugger, C. Morales Morales [17], B. Renk, M. Wache, R. Wanke, A. Winhart
Institut für Physik, Universität Mainz, D-55099 Mainz, Germany [18]

D. Coward [19], A. Dabrowski [8], T. Fonseca Martin [20], M. Shieh, M. Szleper, M. Velasco, M.D. Wood [21]
Department of Physics and Astronomy, Northwestern University, Evanston, IL 60208, USA

P. Cenci, M. Pepe, M.C. Petrucci
Sezione dell'INFN di Perugia, I-06100 Perugia, Italy

G. Anzivino, E. Imbergamo, A. Nappi [4], M. Piccini, M. Raggi [22], M. Valdata-Nappi
Dipartimento di Fisica dell'Università e Sezione dell'INFN di Perugia, I-06100 Perugia, Italy

C. Cerri, R. Fantechi
Sezione dell'INFN di Pisa, I-56100 Pisa, Italy

G. Collazuol [23], L. DiLella, G. Lamanna [8], I. Mannelli, A. Michetti
Scuola Normale Superiore e Sezione dell'INFN di Pisa, I-56100 Pisa, Italy

F. Costantini, N. Doble, L. Fiorini [24], S. Giudici, G. Pierazzini, M. Sozzi, S. Venditti
Dipartimento di Fisica dell'Università e Sezione dell'INFN di Pisa, I-56100 Pisa, Italy

B. Bloch-Devaux [25], C. Cheshkov [26], J.B. Chèze, M. De Beer, J. Derré, G. Marel, E. Mazzucato, B. Peyaud, B. Vallage
DSM/IRFU – CEA Saclay, F-91191 Gif-sur-Yvette, France

M. Holder, M. Ziolkowski
Fachbereich Physik, Universität Siegen, D-57068 Siegen, Germany [27]

C. Biino, N. Cartiglia, F. Marchetto
Sezione dell'INFN di Torino, I-10125 Torino, Italy

S. Bifani [28], M. Clemencic [8], S. Goy Lopez [29]
Dipartimento di Fisica Sperimentale dell'Università e Sezione dell'INFN di Torino, I-10125 Torino, Italy

H. Dibon, M. Jeitler, M. Markytan, I. Mikulec, G. Neuhofer, L. Widhalm
Österreichische Akademie der Wissenschaften, Institut für Hochenergiephysik, A-10560 Wien, Austria [30]

[1] University of Birmingham, Edgbaston, Birmingham, B15 2TT, UK
[2] Funded by the UK Particle Physics and Astronomy Research Council
[3] Università degli Studi del Piemonte Orientale e Sezione dell'INFN di Torino, I-10125 Torino, Italy
[4] Deceased
[5] Istituto di Cosmogeofisica del CNR di Torino, I-10133 Torino, Italy
[6] Dipartimento di Fisica dell'Università e Sezione dell'INFN di Ferrara, I-44100 Ferrara, Italy
[7] Department of Physics, Imperial College, London, SW7 2BW, UK
[8] CERN, CH-1211 Genève 23, Switzerland
[9] Physikalisches Institut, Ruprecht-Karls-Universität Heidelberg, D-69120 Heidelberg, Germany
[10] Faculty of Physics, University of Sofia "St. Kl. Ohridski", 1164 Sofia, Bulgaria, funded by the Bulgarian National Science Fund under contract DID02-22
[11] Northwestern University, Evanston, IL 60208, USA
[12] Centre de Physique des Particules de Marseille, IN2P3-CNRS, Université de la Méditerranée, F-13288 Marseille, France
[13] Department of Physics and Astronomy, George Mason University, Fairfax, VA 22030, USA
[14] CP3, Université Catholique de Louvain, B-1348 Louvain-la-Neuve, Belgium
[15] Dipartimento di Fisica, Università di Modena e Reggio Emilia, I-41125 Modena, Italy
[16] Istituto di Fisica, Università di Urbino, I-61029 Urbino, Italy
[17] Helmholtz-Institut Mainz, Universität Mainz, D-55099 Mainz, Germany
[18] Funded by the German Federal Minister for Education and research under contract 05HK1UM1/1
[19] SLAC, Stanford University, Menlo Park, CA 94025, USA
[20] Laboratory for High Energy Physics, CH-3012 Bern, Switzerland
[21] UCLA, Los Angeles, CA 90024, USA
[22] Laboratori Nazionali di Frascati, via E. Fermi, 40, I-00044 Frascati (Rome), Italy
[23] Dipartimento di Fisica dell'Università e Sezione dell'INFN di Padova, I-35131 Padova, Italy
[24] Instituto de Física Corpuscular IFIC, Universitat de València, E-46071 València, Spain
[25] Dipartimento di Fisica Sperimentale dell'Università di Torino, I-10125 Torino, Italy
[26] Institut de Physique Nucleaire de Lyon, IN2P3-CNRS, Universite Lyon I, F-69622 Villeurbanne, France
[27] Funded by the German Federal Minister for Research and Technology (BMBF) under contract 056SI74
[28] University College Dublin School of Physics, Belfield, Dublin 4, Ireland
[29] Centro de Investigaciones Energeticas Medioambientales y Tecnologicas, E-28040 Madrid, Spain
[30] Funded by the Austrian Ministry for Traffic and Research under the contract GZ 616.360/2-IV GZ 616.363/2-VIII, and by the Fonds für Wissenschaft und Forschung FWF Nr. P08929-PHY

1 Introduction

The interest of $K^{\pm} \to \pi^+\pi^- e^{\pm}\nu$ decays (denoted K_{e4} in the following) was recognized many years ago at a time when only a handful of such events had been observed [1]. The accumulation of a large sample of more than one million of such decays by the NA48/2 experiment has recently allowed a very detailed study of the $\pi\pi$ scattering lengths and hadronic form factors [2]. In that study, the $I = 0$ and $I = 2$ S-wave scattering lengths have been determined with an improved precision comparable to the few percent relative accuracy of the most elaborate theoretical predictions [3]. Without the branching ratio value, only relative form factors could be measured, giving a full set of values up to a common normalization.

A new measurement of the K^+_{e4} and K^-_{e4} decay rates based on the data collected by the NA48/2 experiment at the CERN SPS in 2003–2004 is reported here. The event sample is about three times larger than the total world sample and has one percent level background contamination. A good control of systematic uncertainties, dominated by the external error from the normalization mode, allows rate and form factors to be measured with an improved precision. These can be used as input to the determination of the Low Energy Constants (LEC) of Chiral Perturbation Theory (ChPT) [4, 5, 6] and as tests of other theoretical dispersive approaches [7].

2 The NA48/2 experiment beam and detector

The NA48/2 experiment, specifically designed for charge asymmetry measurements [8], takes advantage of simultaneous K^+ and K^- beams produced by 400 GeV/c primary CERN SPS protons impinging on a 40 cm long beryllium target. Oppositely charged particles, with a central momentum of 60 GeV/c and a momentum band of $\pm 3.8\%$ (rms), are selected by two systems of dipole magnets with zero total deflection (each system forming an 'achromat'), focusing quadrupoles, muon sweepers and collimators.

At the entrance of the decay volume housed in a 114 m long evacuated vacuum tank, the beams contain $\sim 3.6 \times 10^6$ charged kaons per pulse of about 4.5 s duration with a flux ratio K^+/K^- close to 1.8. Both beams follow the same path in the decay volume: their axes coincide within 1 mm, while the transverse size of each beam is about 1 cm.

The decay volume is followed by a magnetic spectrometer located in a tank filled with helium at nearly atmospheric pressure, separated from the vacuum tank by a thin ($0.3\%X_0$) Kevlar® window. An aluminum beam pipe of 16 cm outer diameter traversing the centre of the spectrometer (and all the following detector elements) allows the undecayed beam particles and the muon halo from decays of beam pions to continue their path in vacuum. The spectrometer consists of four octagonal drift chambers (DCH), each composed of four staggered double planes of sense wires, and located upstream (DCH1–2) and downstream (DCH3–4) of a large aperture dipole magnet. The magnet provides a transverse momentum kick $\Delta p = 120$ MeV/c to charged particles in the horizontal plane. The momentum resolution achieved in the spectrometer is $\sigma_p/p = (1.02 \oplus 0.044 \cdot p)\%$ (p in GeV/c).

The spectrometer is followed by a hodoscope (HOD) consisting of two planes of plastic scintillator segmented into vertical and horizontal strip-shaped counters (128 in total). The HOD surface is logically subdivided into 16 exclusive square regions whose fast signals are used to trigger the detector readout on charged track topologies. Its time resolution is ~ 150 ps.

A liquid krypton electromagnetic calorimeter (LKr), used for particle identification in the present analysis, is located behind the HOD. It is an almost homogeneous ionization chamber with an active volume of 7 m^3 of liquid krypton, segmented transversally into 13248 projective cells, approximately 2×2 cm^2 each, $27X_0$ deep and with no longitudinal segmentation. The energies of electrons and photons are measured with a resolution $\sigma_E/E = (3.2/\sqrt{E} \oplus 9.0/E \oplus$

0.42)% (E in GeV) and the transverse position of isolated showers is measured with a spatial resolution $\sigma_x = \sigma_y = (0.42/\sqrt{E} \oplus 0.06)$ cm.

The muon veto counter (MUV) is located further downstream. It is composed of three planes of plastic scintillator slabs (aligned horizontally in the first and last planes, and vertically in the middle plane) read out by photomultipliers at both ends, each preceded by a 0.8 m thick iron absorber. The MUV is also preceded by a hadronic calorimeter (not used in this analysis) with a total iron thickness of 1.2 m.

A more detailed description of the NA48 detector and its performances can be found in [9].

A dedicated two-level trigger selects and flags the events. At the first level (L1), charged track topologies are selected by requiring coincidences of hits in the two HOD planes in at least two of the 16 square regions. At the second level (L2), a farm of asynchronous microprocessors performs a fast reconstruction of tracks and runs a decision-taking algorithm. This trigger logic ensures a very high trigger efficiency for three-track topologies. Inefficiencies are typically a few 10^{-3} at the first level and a few 10^{-2} at the second level (more details can be found in [2, 8]).

3 Branching ratio measurement

The K_{e4} rate is measured relative to the abundant $K^{\pm} \to \pi^+\pi^-\pi^{\pm}$ normalization channel (denoted $K_{3\pi}$ below). As the topologies of the two modes are similar in terms of number of charged particles, the two samples are collected concurrently using the same trigger logic and a common event selection is considered as far as possible. This leads to partial cancellation of the systematic effects induced by an imperfect kaon beam description, local detector inefficiencies and a trigger inefficiency. The K_{e4} rate relative to $K_{3\pi}$ and the K_{e4} branching ratio (BR) are obtained as:

$$\Gamma(K_{e4})/\Gamma(K_{3\pi}) = \frac{N_s - N_b}{N_n} \cdot \frac{A_n\ \varepsilon_n}{A_s\ \varepsilon_s} \tag{1}$$

and

$$\mathrm{BR}(K_{e4}) = \frac{N_s - N_b}{N_n} \cdot \frac{A_n\ \varepsilon_n}{A_s\ \varepsilon_s} \cdot \mathrm{BR}(K_{3\pi}), \tag{2}$$

where N_s, N_b, N_n are the numbers of signal, background and normalization candidates (the background in the normalization sample is negligible), A_s and ε_s are the geometrical acceptance and trigger efficiency for the signal sample, A_n and ε_n are those of the normalization sample. The normalization branching ratio value $\mathrm{BR}(K_{3\pi}) = (5.59 \pm 0.04)\%$ is the world average as computed in [10].

It should be noted that the K^-_{e4} rate has never been measured. As no difference is expected from the K^+_{e4} rate [1], a comparison of the separate measurements of the K^+ and K^- rates is used as a consistency check.

3.1 Event selection

The same data sample has been considered in both signal and normalization studies. Given that $\mathrm{BR}(K_{3\pi})/\mathrm{BR}(K_{e4}) \simeq 1400$, a filtering of the data stream and the analysis are performed in such a way that the $K_{3\pi}$ candidates are effectively prescaled by a factor of 100 with a negligible error, while the K_{e4} candidates are not affected, leading to a significant reduction of the data volume.

The analysis of the $\pi\pi$ scattering lengths and form factors presented in [2] focuses on a sample free of hard radiative events at the price of some cuts on the additional photon activity in the LKr calorimeter. The present analysis includes radiative events and thus loosens or removes

some of the selection cuts which could bias the event counting because of imperfect modeling of the photon emission mechanism.

Common selection

Three-track vertices (compatible with either K_{e4} or $K_{3\pi}$ decay topology), in events satisfying the three-track trigger logic conditions, are reconstructed by backward extrapolation of track segments from the spectrometer into the decay volume, taking into account the measured stray magnetic field in the vacuum tank and multiple scattering. The reconstructed vertex must satisfy the following criteria:
— total charge of the three tracks (called "vertex tracks" in the following) equal to ± 1;
— longitudinal position of the vertex within the fiducial decay volume, 2 to 95 m downstream of the final collimator, and its transverse position within 5 cm of the nominal beam axis;
— vertex tracks consistent in time within 12 ns; no additional in-time tracks present in the reconstructed event (see section 3.4 for details);
— all vertex tracks within the DCH, HOD, LKr and MUV geometric acceptances; distance between any track and the beam mean position (monitored with $K_{3\pi}$ decays) in the DCH1 plane greater than 12 cm for better time-dependent acceptance control;
— track separations required in the DCH1 and LKr planes (minimum allowed distance 2 cm and 20 cm respectively) to suppress photon conversions and to ensure efficient particle identification, minimizing shower overlaps;
— distance from the impact point of each vertex track on the LKr plane to the closest inactive cell of the calorimeter larger than 2 cm to provide maximum collection of energy deposit;
— total momentum of the three tracks $|\sum \vec{p}_i|$ below 70 GeV/c;
— no track-associated signal allowed in at least two planes of the MUV in-time with any vertex track (within 10 ns).
If several vertices satisfy the above conditions, the one with the lowest fit χ^2 is considered.

Particle identification

Particle identification criteria are based on the geometric association of an in-time LKr energy deposition cluster to a track extrapolated to the calorimeter front face (denoted "associated cluster" below). The ratio of energy deposition in the LKr calorimeter to momentum measured by the spectrometer (E/p) is used for pion/electron separation. A track is identified as an *electron* ($e^{\pm}$) if its momentum is greater than 2.75 GeV/c and it has an associated cluster with E/p between 0.9 and 1.1. A track is identified as a *pion* ($\pi^{\pm}$) if its momentum is above 5 GeV/c and it has either no associated cluster or an associated cluster with E/p smaller than 0.8.

Powerful further suppression of pions mis-identified as electrons within the above conditions is obtained by using a discriminant variable which is a linear combination of quantities related to shower properties (E/p, radial shower width and energy weighted track-cluster distance at LKr front face), and is almost momentum independent. The discriminant variable was trained on dedicated track samples to be close to 1 for electron tracks and close to 0 for pion tracks faking electron tracks (the discriminant variable performances are shown in section 3.4). In the signal selection, its value is required to be larger than 0.9 for the *electron* track.

Signal sample

The K_{e4} candidates are then selected using the following particle identification and kinematic criteria:
— the vertex is composed of a single *electron* candidate and a pair of oppositely charged *pion* candidates $\pi^+\pi^-$;
— the invariant mass of the three tracks in the $\pi^+\pi^-\pi^{\pm}$ hypothesis ($M_{3\pi}$) and the transverse momentum p_t relative to the beam axis are outside a half-ellipse centered on the nominal kaon

mass [10] and zero p_t, with semi-axes of 20 MeV/c^2 and 35 MeV/c, respectively, thus requiring a non-zero p_t value for the undetected neutrino and rejecting fully reconstructed three-body $K_{3\pi}$ decays (the K_{e4} signal loss from this cut is $\sim 4.5\%$, as shown by simulation);
— the square invariant mass M_X^2 in the $K^\pm \to \pi^\pm X$ decay is larger than 0.04 (GeV/c^2)^2 to reject $K^\pm \to \pi^\pm\pi^0$ decays with a subsequent $\pi^0 \to e^+e^-\gamma$ decay;
— the invariant mass of the e^+e^- system (assigning an electron mass to the oppositely charged pion candidate) is larger than 0.03 GeV/c^2 to ensure rejection of converted photons and of some multi-π^0 events (as $K^\pm \to \pi^\pm\pi^0\pi^0$).

Extra rejection of three-body decays is obtained by reconstructing the kaon momentum under the assumption of a four-body decay with an undetected massless neutrino. Imposing energy-momentum conservation in the decay and fixing the kaon mass and the beam direction to their nominal values, a quadratic equation in the kaon momentum p_K is obtained. A K_{e4} candidate is accepted if a solution is found in the nominal range between 54 and 66 GeV/c, allowing a small fraction of solutions with negative but close to zero equation discriminant values as observed for reconstructed simulated signal events because of non-perfect resolution (in this case, a single solution is obtained by setting the equation discriminant to zero).

A total sample of 1 108 941 K_{e4} candidates (712 288 K^+ and 396 653 K^-) were selected from a total of $\sim 2.5 \times 10^{10}$ triggers recorded in 2003–2004. The selection is illustrated in Fig. 1a in the $(M_{3\pi}, p_t)$ plane and the reconstruction in Fig. 1b by the kaon momentum distribution.

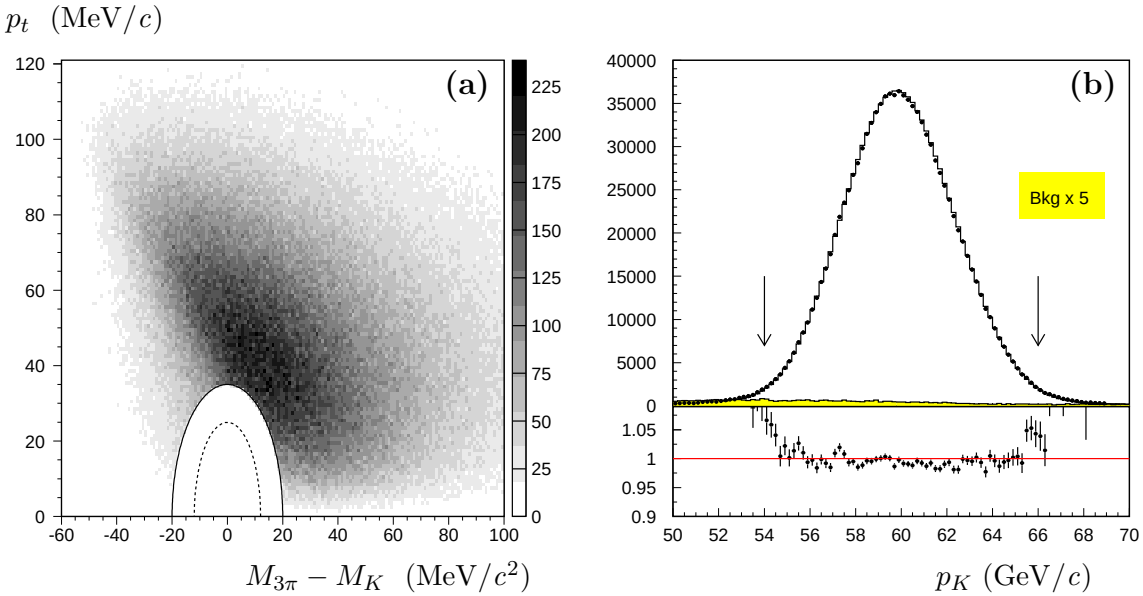

Figure 1: **(a)** Reconstructed $(M_{3\pi}, p_t)$ plane for the K_{e4} signal candidates. The elliptic cuts used in the signal (solid line) and normalization (dashed line) selections are shown. **(b)** Reconstructed kaon momentum from signal events for data after background subtraction (symbols), simulation normalized to data (histogram) and background events (scaled by a factor of 5 to be visible) as shaded area. The arrows point to the kaon momentum cuts values. The lower plot is the ratio of the two spectra (data/simulation) displayed in the upper plot.

Background estimate

The $K_{3\pi}$ decay is the most significant background source. It contributes either via the decay in flight of a single pion ($\pi^\pm \to e^\pm\nu$) or mis-identification of a pion as an electron. Only pion decays occurring close to the kaon decay vertex or leading to a forward electron and thus consistent with a three-track vertex and satisfying the $(M_{3\pi}, p_t)$ requirements contribute to the background. Other background sources come from $K^\pm \to \pi^\pm\pi^0(\pi^0)$ decays with subsequent Dalitz decay of

a π^0 ($\pi^0_D \to e^+e^-\gamma$), an electron mis-identified as a pion, and photon(s) undetected. Such two- or three-body decay topologies are very unfavored by the signal selection criteria and contribute at sub per mil level.

Decays violating the $\Delta S = \Delta Q$ rule would appear as "wrong sign electron" (WS) $\pi^\pm\pi^\pm e^\mp\nu$ K_{e4} candidates and are expected at a negligible rate (BR $< 1.2 \times 10^{-8}$ at 90% confidence level [10]). The kinematic distribution of the background events is then to a good approximation identical to that of the reconstructed WS candidates multiplied by a factor of 2 as two pions from $K_{3\pi}$ decays can mimic the signal final state while one pion only contributes to the WS topology. The uncertainty on this factor of 2 is discussed in section 3.4.

Changing the requirement of a pair of opposite charge pions ($\pi^+\pi^-$ candidates) in the vertex selection to a pair of same charge pions ($\pi^\pm\pi^\pm$ candidates) and keeping all other requirements unchanged is sufficient to determine the number of events in the WS sample. The distribution of the WS K_{e4} candidates in the $(M_{3\pi}, p_t)$ plane is displayed in Fig. 2a. Another feature of the WS sample is shown in Fig. 2b which displays the reconstructed invariant mass of the dilepton system in the signal and WS selections. A peak at the m_{π^+} value can be seen as expected from $K_{3\pi}$ decays followed by a pion decay in flight.

A sample of 5276 K_{e4} WS candidates (3276 K^+ and 2000 K^-) has been selected concurrently with the signal sample. As $K_{3\pi}$ decays are the dominant contributors, the total background is then estimated to be 2×5276 events, a 0.95% relative contamination to the signal. The systematic uncertainty on this quantity is discussed in section 3.4.

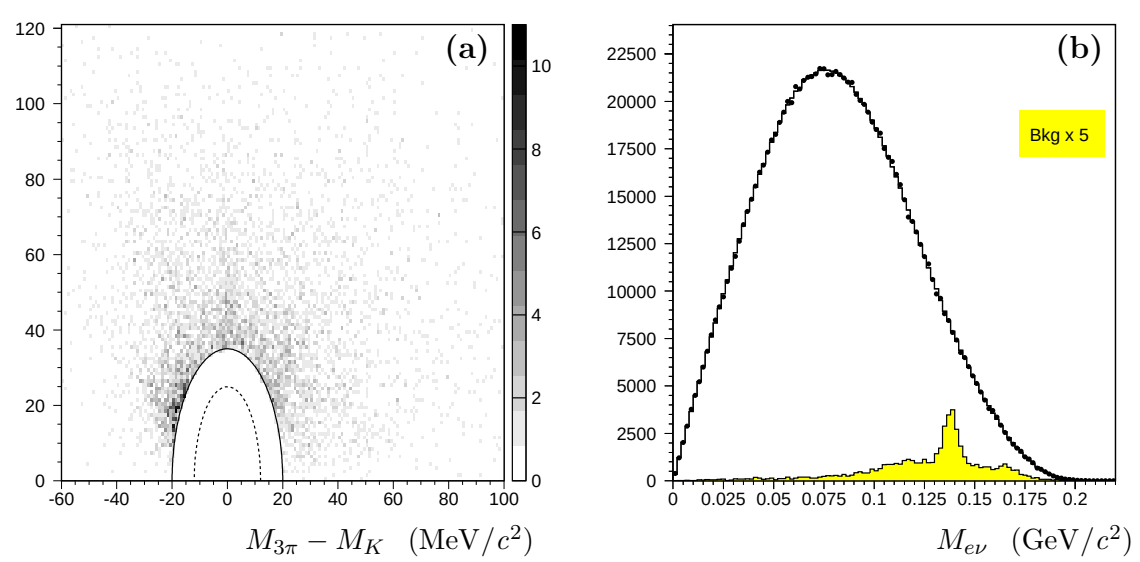

Figure 2: **(a)** Reconstructed $(M_{3\pi}, p_t)$ plane for the K_{e4} background estimated from WS events. The elliptic cuts used in the WS selection (solid line) and normalization (dashed line) selections are shown. **(b)** Reconstructed dilepton invariant mass for K_{e4} events. Data are shown as symbols, simulation as histogram and background events (scaled by a factor of 5 to be visible) as shaded area.

Normalization sample

The $K_{3\pi}$ sample is selected applying the following requirements to events passing the common selection:

— the vertex is required to be composed of three *pion* $\pi^+\pi^-\pi^\pm$ candidates;

— the invariant mass of the three tracks in the $\pi^+\pi^-\pi^\pm$ hypothesis ($M_{3\pi}$) and the transverse momentum p_t are inside a half-ellipse (as drawn in Fig. 1a) centered on the kaon mass and zero p_t, with semi-axes 12 MeV/c^2 and 25 MeV/c, respectively, thus requiring fully reconstructed

$K_{3\pi}$ three-body decays;
— the total momentum of the three tracks $|\sum \vec{p}_i|$ is between 54 and 66 GeV/c.

The reconstructed $M_{3\pi}$ invariant mass spectrum is displayed in Fig. 3a. Its measured resolution $\sigma_{3\pi} = 1.7$ MeV/c^2 is in agreement with simulation. The three track momentum sum distribution is shown in Fig. 3b. The residual disagreement between data and simulation is considered in the systematic uncertainties study.

The number of prescaled $K_{3\pi}$ candidates in the signal region is 18.82×10^6 (12.09×10^6 K^+ and 6.73×10^6 K^-) with a negligible background.

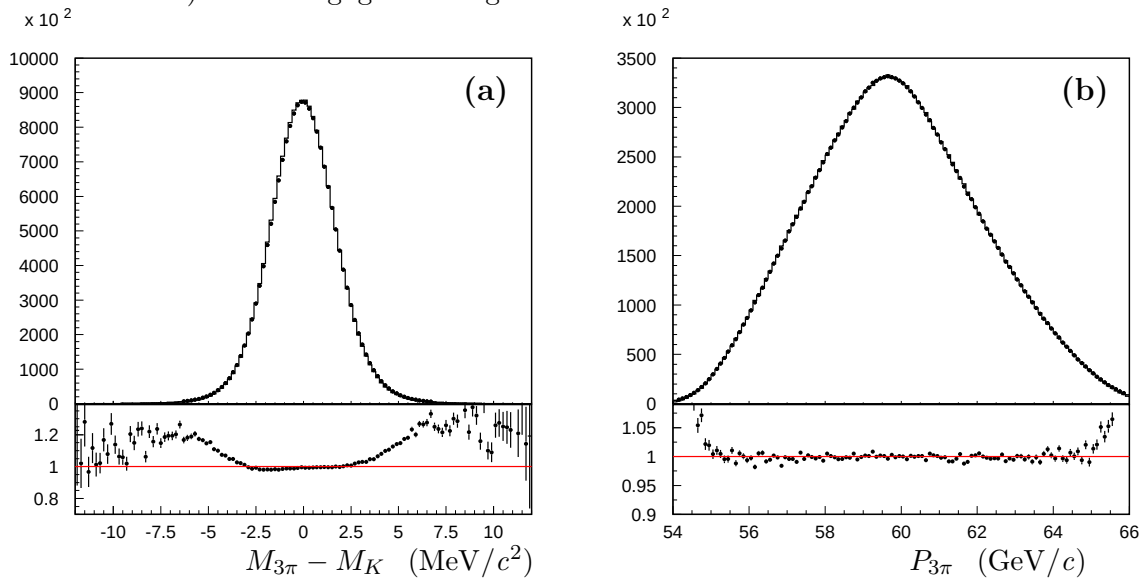

Figure 3: Distributions of the reconstructed $M_{3\pi}$ invariant mass **(a)** and the reconstructed kaon momentum **(b)** for the normalization $K_{3\pi}$ candidates within the final selection. Data are shown as symbols and simulation normalized to data as histograms. The lower plots are the ratios of the distributions (data/simulation) displayed in the upper plots.

3.2 Acceptance calculation

A detailed GEANT3-based [11] Monte Carlo (MC) simulation is used to compute the acceptances for signal and normalization channels. It includes full detector geometry and material description, stray magnetic fields, DCH local inefficiencies and misalignment, LKr local inefficiencies, accurate simulation of the kaon beam line, and time variations of the above throughout the running period. This simulation is used to achieve a large time-weighted MC production, providing a simulated event sample about 20 times larger than the signal sample and 1/4 of the prescaled normalization sample, reproducing the observed flux ratio $(K^+/K^-) \sim 1.8$.

The K_{e4} signal channel is generated according to the most precise description of the form factors as obtained in [2]. The normalization channel $K_{3\pi}$ is well understood in terms of simulation, being of primary physics interest to NA48/2 [8]. The most precise values of the slopes of the Dalitz plot have been implemented [12]. Attraction/repulsion between opposite charge/same charge particles and real photon emission using `PHOTOS` 2.15 [13] are included in both simulations.

The same selection and reconstruction as described in section 3.1 are applied to the simulated events except for the trigger and timing cuts. Particle identification cuts related to the LKr response are replaced by momentum-dependent efficiencies, obtained from pure samples of electron and pion tracks.

The acceptances averaged over periods with different data taking conditions and over the two kaon charges are $(18.193 \pm 0.004)\%$ and $(23.967 \pm 0.010)\%$ for the signal and normalization

channels, respectively. Due to the detector and beam line being largely charge symmetric by design, and due to the data taking conditions, these values are practically identical for K^+ and K^-. The uncertainty on the acceptance calculations due to the limited size of the simulation samples (a few 10^{-4} relative) is included in the systematic error.

3.3 Trigger efficiency

Trigger efficiencies are measured from the data using a minimum bias sample downscaled by 100, recorded concurrently with the main analysis data stream. The control trigger condition for the first level efficiency requires at least one coincidence of hits in the two planes of the scintillator hodoscope (HOD). Control triggers for the second level efficiency consist of first level triggers recorded regardless of the second level decision. The overall trigger efficiency is $(98.52 \pm 0.11)\%$ in the signal channel and $(97.65 \pm 0.03)\%$ in the normalization channel. The observed difference between the two efficiencies can be explained by the different signal and normalization topologies, four-body and three-body decays respectively. Three track events from four-body decays are less affected by first level trigger inefficiencies (two tracks in the same HOD square region) and by local DCH inefficiencies at the second level trigger [8]. The limited statistics of the available control samples have a sizable contribution to the systematic error on the K_{e4} branching ratio measurement.

3.4 Systematic uncertainties

A large number of possible effects have been studied and quantified, many of them being upper limits. When necessary, a correction is applied to account for any observed bias, and residual effects are quoted as systematic uncertainty. The considered contributions are described below.

Acceptance stability. Many studies have been performed varying in turn the value of each cut applied in the common, signal and normalization selections. The maximum deviation observed with respect to the value of the reference cut has been quoted as the uncertainty if statistically significant. None of the studied contributions are dominant and all are below the per mil relative level. Varying the common selection cuts contributes 0.03% to the relative systematic uncertainty of BR(K_{e4}). In the signal selection, the anti-background cuts amount to 0.03% while the p_K cut and residual momentum differences together contribute 0.08%. The normalization selection cuts add another 0.08%. Momentum cuts in the particle identification contribute 0.05% each when considering *electron* and *pion* definitions.

Time control of the beam geometry and acceptance modeling have been investigated in detail. While the acceptances for signal and normalization show a relative variation of ~ 2 percent between different data taking periods, related to beam geometry and DCH local inefficiencies, their ratio is stable in time. A relative change of 0.07% with respect to the nominal result is observed when simulated samples used to compute the acceptances are swapped between subsamples of the data before combining them. This value is assigned as an upper limit of the systematic uncertainty due to time variation of acceptance and beam geometry. It is fully consistent with the variations observed when considering smaller subsamples of the data based on kaon beam charge and polarity of the achromat and spectrometer magnets.

The impact of the limited precision of the measured relative form factors [2] on the signal acceptance has also been considered (0.06%). The modeling of the amount of material seen by decay particles before the magnet could affect bremsstrahlung emission of additional photons. As a result of the absence of explicit cuts on additional LKr activity from photons, the estimated 4% precision on the simulated material thickness has only a 0.06% impact on the final result.

All the above uncertainties have been added in quadrature to a total relative contribution of 0.18%.

Muon vetoing efficiency. The MUV veto requirement in the common selection (Section 3.1) is essential in suppressing the $K_{3\pi}$ background to an acceptable level[1]. Removing the MUV requirement in the selection of simulated signal and normalization events increases both acceptance values, but their ratio A_n/A_s remains unchanged within 0.05%, suggesting that the rejection of late pion decays in flight does not bias the result. The probability to reconstruct a common three-track vertex decreases significantly when one or more pions decay to muons. The potential effect of the different number of final state pions in signal and normalization channels is therefore minimized at the level of the common selection by requiring the presence of a good quality vertex. Stability of the result with respect to muon vetoing is also supported by varying the minimum track momentum cut from the nominal 5 GeV/c up to 10 GeV/c, where the efficiency of MUV hit reconstruction varies by more than 10% while the relative change of the final result is within 0.05%.

In order to estimate the potential bias from MUV reconstruction algorithm and combinatorial effects, the requirement for MUV hit association in the common selection has been modified to reject events with hits in all three rather than in at least two MUV planes. The observed 0.16% relative difference is conservatively quoted as a systematic uncertainty.

Accidental activity. Possible accidental activity, either from beam particles or from fake tracks (*ghost* tracks) resulting from DCH hit combinatorics[2], has been subjected to a dedicated study.

The difference Δt between the time of each vertex track and their average (the vertex time) is required to be within ± 6 ns in the common selection. Removing this requirement reveals different tails in Δt distribution for $K_{3\pi}$ and K_{e4} selections suggesting different contributions of accidental tracks forming a good vertex. The bias due to this effect is estimated by extrapolation from the control regions (–16; –10) ns and (+10; +16) ns to the nominal time window (accounting for WS events) as illustrated in Fig. 4a. The subtraction of accidental background leads to a -0.12% correction to the result, and the difference between two estimates (based on constant and parabolic extrapolation to the central signal window) is quoted as its uncertainty (0.06%).

An event is rejected if an extra *non-ghost* track is present within a 6 ns window around the three-track vertex time. A conservative estimate of the uncertainty due to the presence of accidental tracks not forming the decay vertex is obtained by variation of the above time limit up to 35 ns, and it is found to be 0.21%.

Ghost tracks are not allowed to form an accepted vertex and their presence in addition to the considered tracks is ignored in order to avoid bias in $K_{3\pi}$ and K_{e4} samples related to the different reconstruction probabilities of fake tracks from pions and electrons. The *ghost* track tagging procedure using modified criteria (distance between tracks and quality of track reconstruction) has been studied in detail to identify the optimal one, and the residual systematic bias is estimated to be 0.04%.

Particle identification. Different *pion* identification requirements have been studied, relaxing the E/p condition and recomputing signal and normalization acceptances as described in section 3.2. The largest difference to the reference result (0.08%) is quoted as the related uncertainty. For the *electron* identification, varying the cut on the linear discriminant variable value between 0.85 and 0.95 (or even removing the cut) changes drastically the background contamination (up to a factor of four). Applying the corresponding momentum-dependent efficiency (Fig. 4b) to the simulation, no bias is observed and a maximum deviation of 0.04% from the reference result (obtained for the cut value of 0.90) is observed. The uncertainties from *pion* and *electron* identification are added quadratically.

Background estimate. The uncertainty on the scaling factor of 2 used to estimate the

[1]The background increases by a factor of 10 when this requirement is removed.

[2]A *ghost* track is close to another track by less than 1 cm at the DCH1 plane and is reconstructed with worse quality.

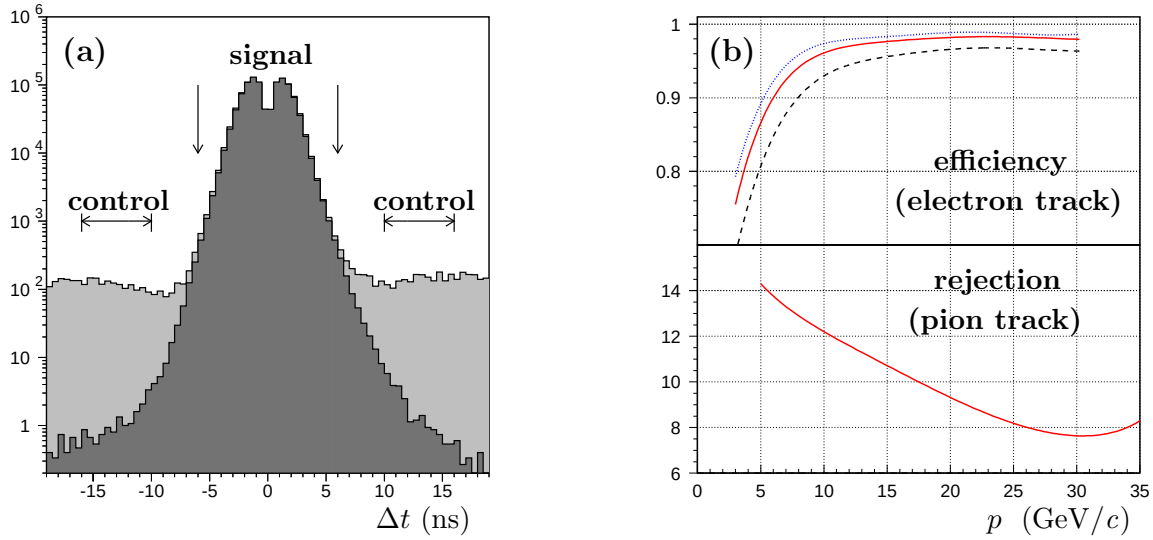

Figure 4: **(a)** Normalized distribution of the time difference between the time of each vertex track and their average for K_{e4} (light shaded area) and $K_{3\pi}$ (dark shaded area) candidates. The vertical arrows indicate the signal time window. The horizontal arrows indicate the two control regions. Only the time difference of the track with the largest Δt absolute value is plotted. **(b)** Efficiency of the linear discriminant variable as a function of momentum for electron tracks (top curves). The solid line corresponds to the cut value of 0.90 applied in this analysis. The lower dashed line corresponds to the cut value of 0.95 and the upper dotted line to the cut value of 0.85. For illustration, the pion track rejection (bottom curve) is displayed for the cut value of 0.90.

background based on WS K_{e4} candidates has been studied in two ways. In the WS event selection, the square invariant mass M_X^2 (Section 3.1) is computed for both pions and can be used to classify further the origin of the event. If the smaller mass squared is above $(0.27\ \mathrm{GeV}/c^2)^2$ (corresponding to $2m_{\pi^+}$ with resolution smearing), the event is assigned a factor two weight as being $K_{3\pi}$-like (95.8%), otherwise it is assigned a factor one weight as being $K_{\pi\pi^0_D}$-like (4.2%). This rough estimate leads to a factor 1.96. Another estimate, based on a simulated $K_{3\pi}$ sample properly weighted for particle-identification performances, gives a similar ratio Right Sign electron/Wrong Sign electron $= (1.94 \pm 0.15)$, confirming the prescription for WS background related to pion misidentification. It is also in agreement with the overall factor of (2.0 ± 0.3) used in the form factor analysis [2]. The ± 0.15 uncertainty is propagated to the result as a relative uncertainty of 0.07%, based on the above studies. In addition, variation of the background-related requirements in the K_{e4} selection within wide ranges shows excellent stability of the result.

Other sources. Dedicated MC samples simulated without real photon emission were used to estimate the impact from radiative effects description. One tenth of the full effect was assigned as a modeling uncertainty according to the prescription of [14].

Trigger efficiency accuracy is limited by the size of the control samples. The statistical precision is quoted as a contribution to the systematic uncertainty.

Simulated samples used in the acceptance calculations contribute to the systematic uncertainty through their statistical precision: this source could be reduced by increasing the simulation statistics but already contributes at a very low level.

Sizable uncertainty arises from the external input BR($K_{3\pi}$) known experimentally with a limited relative precision of 0.72% [10].

Two independent analyses have been compared on a subsample of the data and found to be

fully consistent, ensuring the robustness of the procedure.

The breakdown of the considered systematic uncertainties is displayed in Table 1.

Table 1: Summary of the relative corrections applied to the BR(K_{e4}) value and relative contributions to the systematic uncertainty.

Source	Correction (%) to BR value	Contribution (%) to BR uncertainty
Common to all subsamples		
Acceptance stability	–	0.18
Muon vetoing efficiency	–	0.16
Accidental activity	–0.12	0.21
Particle identification	–	0.09
Background estimate	–	0.07
Radiative events modeling	–	0.08
Subsample-dependent quoted as a global equivalent		
Trigger efficiency	–	0.11
Simulation statistics	–	0.05
Total systematics	–0.12	0.37
External error	–	0.72

3.5 Results

The final result is a weighted average of 16 values obtained in eight independent data subsamples and both kaon charges. The weight of each input includes error contributions of time-dependent statistical origin: event statistics (signal, background and normalization), trigger efficiencies and acceptances. This method is more robust against time-dependent conditions than using an averaged acceptance and trigger efficiency over the whole data taking period. However, due to the careful time-dependent treatment of simulated samples, this potential difference is kept below the per mil relative level and is taken into account in the systematic error. Other systematic uncertainties (Table 1) are common to all subsamples and are then quoted as a single error on the final result. All input ingredients to the BR(K_{e4}) measurement are summarized in Table 2. By convention, the uncertainties are assigned to three categories: (i) statistical errors from the numbers of K_{e4} signal candidates (dominant error), WS data events (used for background computation) and normalization events; (ii) subsample-dependent systematic uncertainties such as those of trigger efficiencies and acceptance and systematic uncertainties common to all subsamples; (iii) the external error related to the uncertainty on the normalization mode branching ratio (BR($K_{3\pi}$) = $(5.59 \pm 0.04)\%$ [10]).

The resulting values, including all errors, are found to be:

$$\Gamma(K_{e4})/\Gamma(K_{3\pi}) = (7.615 \pm 0.008_{\rm stat} \pm 0.028_{\rm syst}) \times 10^{-4} \tag{3}$$

and

$$\mathrm{BR}(K_{e4}) = (4.257 \pm 0.004_{\rm stat} \pm 0.016_{\rm syst} \pm 0.031_{\rm ext}) \times 10^{-5}, \tag{4}$$

where the branching ratio error is dominated by the external uncertainty from the normalization mode. The BR(K_{e4}) values obtained for the statistically independent subsamples are shown in Fig. 5, also in perfect agreement with the global value obtained from the whole sample and the values measured separately for K^+ and K^-:

$$\mathrm{BR}(K^+_{e4}) = (4.255 \pm 0.008) \times 10^{-5}, \quad \mathrm{BR}(K^-_{e4}) = (4.261 \pm 0.011) \times 10^{-5},$$

where the quoted uncertainties include statistical and time-dependent systematic contributions.

Table 2: Inputs to the BR(K_{e4}) measurement for K^+, K^- and combined $K^\pm$. The relative contribution of each item to the BR($K^\pm_{e4}$) statistical uncertainty is also shown in the last column. Statistical errors on the acceptance and trigger efficiency values (given within parentheses) are taken into account in the systematic error (Table 1) and not in the total statistical error given in the last row.

	K^+	K^-	$K^\pm$	BR($K^\pm_{e4}$) relative error (%)
Signal events	712 288	396 653	1 108 941	0.096
WS events	3 276	2 000	5 276	0.013
Normalization events/100	12 090 376	6 728 544	18 818 920	0.023
K_{e4} acceptance (%)	18.190	18.197	18.193	(0.020)
$K_{3\pi}$ acceptance (%)	23.970	23.961	23.967	(0.041)
K_{e4} trigger efficiency (%)	98.546	98.480	98.523	(0.108)
$K_{3\pi}$ trigger efficiency (%)	97.634	97.687	97.653	(0.033)
Total relative statistical error (%)				0.100

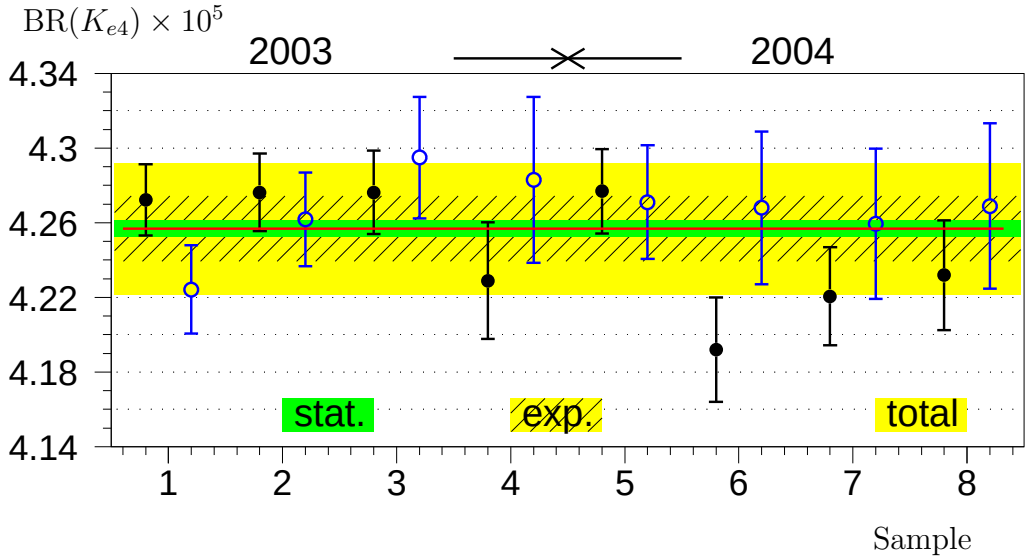

Figure 5: K_{e4} branching ratio for eight statistically independent samples and both kaon charges. The hatched band shows the experimental error ($\sigma_{\rm exp} = \sigma_{\rm stat} \oplus \sigma_{\rm syst}$). The total error (shaded band) includes the external error. The fit χ^2 is 15.85 for 15 degrees of freedom when including the time-dependent errors only. Full symbols correspond to K^+ results and empty symbols to K^- results.

4 Form factors normalization measurement

4.1 Formalism

The K_{e4} decay rate (in s^{-1}) is described in the five-dimensional space of the Cabibbo–Maksymowicz kinematic variables [15], namely the dipion (S_π) and dilepton (S_e) squared invariant masses and the three decay angles [$\theta_\pi(\theta_e)$, the same sign pion (electron) angle in the dipion (dilepton) rest frame to the dipion (dilepton) line of flight in the kaon rest frame, and ϕ, the angle between the dipion and dilepton planes in the kaon rest frame] as:

$$d\Gamma_5 = \frac{G_F^2|V_{us}|^2}{2\hbar(4\pi)^6 m_K^5}\ \rho(S_\pi,S_e)\ J_5(S_\pi,S_e,\cos\theta_\pi,\cos\theta_e,\phi)\ dS_\pi\ dS_e\ d\cos\theta_\pi\ d\cos\theta_e\ d\phi, \qquad (5)$$

where $\rho(S_\pi,S_e) = X\sigma_\pi\,(1-z_e)$ is the phase space factor, with $X = \frac{1}{2}\lambda^{1/2}(m_K^2,S_\pi,S_e)$, $\sigma_\pi = (1-4m_\pi^2/S_\pi)^{1/2}$, $z_e = m_e^2/S_e$ and $\lambda(a,b,c) = a^2+b^2+c^2-2(ab+ac+bc)$. The function J_5, using four combinations of $F,\ G,\ R,\ H$ complex hadronic form factors ($F_i, i=1,4$), reads [16]:

$$\begin{aligned} J_5 = 2(1-z_e)\quad & (I_1 + I_2\,\cos 2\theta_e + I_3\,\sin^2\theta_e\cdot\cos 2\phi + I_4\,\sin 2\theta_e\cdot\cos\phi + I_5\,\sin\theta_e\cdot\cos\phi \\ & + I_6\,\cos\theta_e + I_7\,\sin\theta_e\cdot\sin\phi + I_8\,\sin 2\theta_e\cdot\sin\phi + I_9\,\sin^2\theta_e\cdot\sin 2\phi), \end{aligned}$$

where

$$\begin{aligned} I_1 &= \tfrac{1}{4}\ \left((1+z_e)|F_1|^2 + \tfrac{1}{2}(3+z_e)(|F_2|^2+|F_3|^2)\,\sin^2\theta_\pi + 2z_e|F_4|^2\right), \\ I_2 &= -\tfrac{1}{4}\ (1-z_e)\left(|F_1|^2 - \tfrac{1}{2}(|F_2|^2+|F_3|^2)\,\sin^2\theta_\pi\right), \\ I_3 &= -\tfrac{1}{4}\ (1-z_e)\,(|F_2|^2-|F_3|^2)\ \sin^2\theta_\pi, \\ I_4 &= \tfrac{1}{2}\ (1-z_e)Re(F_1^*F_2)\,\sin\theta_\pi, \\ I_5 &= -\ (Re(F_1^*F_3) + z_e\ Re(F_4^*F_2))\ \sin\theta_\pi, \\ I_6 &= -\ \left(Re(F_2^*F_3)\,\sin^2\theta_\pi - z_e\ Re(F_1^*F_4)\right), \\ I_7 &= -\ (Im(F_1^*F_2) + z_e\ Im(F_4^*F_3))\ \sin\theta_\pi, \\ I_8 &= \tfrac{1}{2}\ (1-z_e)\ Im(F_1^*F_3)\,\sin\theta_\pi, \\ I_9 &= -\tfrac{1}{2}(1-z_e)\ Im(F_2^*F_3)\,\sin^2\theta_\pi. \end{aligned}$$

In K_{e4} decays, the electron mass can be neglected ($z_e = 0$) and the terms $(1 \pm z_e)$ become unity. One should also note that the form factor F_4 is always multiplied by z_e and thus does not contribute to the full expression[3]. With this simplification, the complex hadronic form factors F_i reduce to:

$$F_1 = m_K^2(\gamma\ F + \alpha\ G\,\cos\theta_\pi), \quad F_2 = m_K^2(\beta\ G), \quad F_3 = m_K^2(\beta\gamma\ H), \qquad (6)$$

where one uses the three dimensionless complex form factors F, G (axial), H (vector), and three dimensionless combinations of the S_π and S_e invariants:

$$\alpha = \sigma_\pi(m_K^2 - S_\pi - S_e)/2m_K^2, \quad \beta = \sigma_\pi(S_\pi S_e)^{1/2}/m_K^2, \quad \gamma = X/m_K^2.$$

A further partial wave expansion of the form factors $F_{1,2,3}$ with respect to the $\cos\theta_\pi$ variable is considered [16] and, once limited to S- and P-wave terms and assuming the same phase δ_p for

[3]The form factor R enters only in the definition of F_4 and therefore cannot be addressed in the K_{e4} decay analysis

all P-wave form factors, leads to the expressions for F, G, H:

$$\begin{aligned} F &= F_s\ e^{i\delta_s} + F_p\ e^{i\delta_p}\cos\theta_\pi\ , \\ G &= G_p\ e^{i\delta_p}\ , \\ H &= H_p\ e^{i\delta_p}\ . \end{aligned} \tag{7}$$

The model-independent analysis in [2] determines simultaneously the four real numbers F_s, F_p, G_p, H_p and the phase difference ($\delta = \delta_s - \delta_p$) in bins of S_π, S_e.

In presence of electromagnetic interaction, the differential decay rate (5) is modified by the presence of virtual and real photon emission. This effect is implemented in two steps. First, the Coulomb attraction/repulsion between two opposite/same charge particles is considered:

$$C(S_{ij}) = \prod_{i \neq j} \frac{\omega_{ij}}{e^{\omega_{ij}} - 1}$$

with $\omega_{ij} = 2\pi\alpha Q_i Q_j/\beta_{ij}$, where α is the fine structure constant, $Q_i Q_j = -1$ for opposite charge particles ($+1$ for same charge particles) and β_{ij} is their relative velocity (in units of c). The largest effect comes from the attraction between the two pions at low relative velocity. It depends only on the S_π variable. The electron (positron) being relativistic, the other attractive/repulsive pion-electron terms are constant and their product amounts to 0.9998. Then, the `PHOTOS` 2.15 program [13] interfaced to the simulation is used for real photon emission. Its effect is a distortion of the kinematic variable distributions and is evaluated on a grid of the 5-dimensional space.

4.2 Form factor determination

The K_{e4} decay form factors were extensively studied [2] with the same data sample as used for the present analysis and their energy variation described as a series expansion of the dimensionless invariants $q^2 = (S_\pi/4m_\pi^2) - 1$ and $S_e/4m_\pi^2$. All values have been given relative to a common value f_s, the S-wave axial vector form factor $F_s(q^2 = 0, S_e = 0)$:

$$\begin{aligned} F_s/f_s &= 1 + f_s'/f_s\ q^2 + f_s''/f_s\ q^4 + f_e'/f_s\ S_e/4m_\pi^2\ , \\ F_p/f_s &= f_p/f_s\ , \\ G_p/f_s &= g_p/f_s + g_p'/f_s\ q^2, \\ H_p/f_s &= h_p/f_s\ . \end{aligned} \tag{8}$$

Integrating $d\Gamma_5$ (5) over the 5-dimensional space after substituting F_1, F_2, F_3 (6) by their expression and measured values (7, 8), including radiative effects and leaving out the $|V_{us}|$ and f_s constants, the K_{e4} branching ratio, inclusive of radiative decays, is obtained as:

$$\mathrm{BR}(K_{e4}) = \tau_{K^\pm} \cdot (|V_{us}| \cdot f_s)^2 \cdot \int d\Gamma_5\ /\ (|V_{us}| \cdot f_s)^2, \tag{9}$$

where $\tau_{K^\pm}$ is the $K^\pm$ mean lifetime (in seconds). The value of f_s is then obtained from the measured value of $\mathrm{BR}(K_{e4})$ and the integration result.

Because of the quadratic dependencies displayed in (9), the relative uncertainty on f_s is only half the relative uncertainty from $\mathrm{BR}(K_{e4})$, kaon lifetime and kinematic space integral, while any relative uncertainty on V_{us} propagates with full size. Contributions are categorized as follows:

— Statistical error stems only from the $\mathrm{BR}(K_{e4})$ measurement.

— Systematic uncertainties originate from the $\mathrm{BR}(K_{e4})$ measurement and the phase space integral evaluation. Uncertainties on the integration result when varying each relative form factor

and energy dependence within $\pm 1\sigma$ have been considered. The known large anti-correlations between f_s', f_s'' and g_p, g_p' have been omitted to be conservative. The detailed description of the phase shift between S- and P-wave form factors (7) has a negligible impact. The robustness of the integration method has also been checked against several integration grid definitions. As in the branching ratio and relative form factor measurements, one tenth of the full PHOTOS effect is assigned as systematic uncertainty on the radiative corrections modeling.

— External inputs contributing to the f_s form factor uncertainty are related to the kaon lifetime $\tau_{K^\pm}$, the branching ratio of the normalization decay mode $\mathrm{BR}(K_{3\pi})$ and the $|V_{us}|$ value. All quantities are taken from [10]. However, it should be kept in mind that only the product $|V_{us}| \cdot f_s$ is accessible by this measurement.

Table 3 summarizes the error contributions.

Table 3: Summary of the contributions to the f_s form factor uncertainties.

Source	relative contribution (%)
$\mathrm{BR}(K_{e4})$ statistical error	0.05
$\mathrm{BR}(K_{e4})$ systematic error	0.20
Form factor energy dependence (systematic error)	0.21
Integration method (systematic error)	0.02
Radiative effects in integration (systematic error)	0.04
Total experimental error	0.30
$\mathrm{BR}(K_{e4})$ external error	0.36
Kaon lifetime (external error)	0.08
$\lvert V_{us}\rvert$ (external error)	0.40
Total error (including external errors)	0.62

4.3 Results and discussion

Given the measured K_{e4} branching ratio value (4) and using the world average kaon lifetime value $(1.2380 \pm 0.0021) \times 10^{-8}$ s, the measurement of the form factors [2] is now complemented by the overall f_s normalization:

$$|V_{us}| \cdot f_s = \quad 1.285 \pm 0.001_{\mathrm{stat}} \pm 0.004_{\mathrm{syst}} \pm 0.005_{\mathrm{ext}} \tag{10}$$

$$\text{corresponding to } f_s = \quad 5.705 \pm 0.003_{\mathrm{stat}} \pm 0.017_{\mathrm{syst}} \pm 0.031_{\mathrm{ext}} \tag{11}$$

when using $|V_{us}| = 0.2252 \pm 0.0009$ [10].

The obtained f_s value and its error can be propagated to all relative form factors now displayed with absolute values in Table 4 and including an additional normalization error, fully correlated over all measured values.

In addition to the above set of values, it can be of further theoretical interest to quote also the S- and P-wave normalized projections of the F_1 form factor:

$$F_1/\gamma m_K^2 = F_s \; e^{i\delta_s} + (F_p + \alpha/\gamma \; G_p) \cos\theta_\pi \; e^{i\delta_p}, \tag{12}$$

namely F_s and $(F_p + \alpha/\gamma \; G_p)$, respectively. As all form factors are obtained in simultaneous fits together with the phase difference $\delta_s - \delta_p$ [2], they exhibit correlations which vary with energy. In particular, the fit parameters F_p and G_p are strongly anti-correlated with a coefficient close to unity. The combination $\tilde{G}_p = G_p + \gamma/\alpha \; F_p$ shows much less correlation with G_p (~ 0.20 at most) and is also obtained in the fit. To allow an easy interpretation of the results without the

Table 4: Absolute values of the form factor measurements (as defined in (8)). There are large anti-correlations between f'_s, f''_s (-0.954) and g_p, g'_p (-0.914). The normalization error is fully correlated over all form factors.

f_s	$=$	$5.705 \pm$	$0.003_{\rm stat} \pm$	$0.017_{\rm syst} \pm$	$0.031_{\rm ext}$
f_s	$=$	$5.705 \pm$	$0.035_{\rm norm}$		
f'_s	$=$	$0.867 \pm$	$0.040_{\rm stat} \pm$	$0.029_{\rm syst} \pm$	$0.005_{\rm norm}$
f''_s	$=$	$-0.416 \pm$	$0.040_{\rm stat} \pm$	$0.034_{\rm syst} \pm$	$0.003_{\rm norm}$
f'_e	$=$	$0.388 \pm$	$0.034_{\rm stat} \pm$	$0.040_{\rm syst} \pm$	$0.002_{\rm norm}$
f_p	$=$	$-0.274 \pm$	$0.017_{\rm stat} \pm$	$0.023_{\rm syst} \pm$	$0.002_{\rm norm}$
g_p	$=$	$4.952 \pm$	$0.057_{\rm stat} \pm$	$0.057_{\rm syst} \pm$	$0.031_{\rm norm}$
g'_p	$=$	$0.508 \pm$	$0.097_{\rm stat} \pm$	$0.074_{\rm syst} \pm$	$0.003_{\rm norm}$
h_p	$=$	$-2.271 \pm$	$0.086_{\rm stat} \pm$	$0.046_{\rm syst} \pm$	$0.014_{\rm norm}$

explicit description of the fit correlations, the values of $F_s,\ \tilde{G}_p$ are given in Table 5 together with those of F_p, G_p and H_p. Using (12), the P-wave F_1 normalized projection can then be obtained as $\alpha/\gamma\ \tilde{G}_p$. It can be noted that for $S_e = 0$, the factor α/γ reduces to σ_π.

Table 5: Absolute values of form factor measurements in ten $M_{\pi\pi}$ bins. First error within parentheses is statistical, second is systematic (bin to bin uncorrelated part only). A common relative error of 0.62% must be added to each form factor bin by bin measurement, fully correlated over all form factor and bin measurements. F_s values correspond to the projection of $F_s(S_\pi, S_e)$ on the $M_{\pi\pi}$ axis. No significant S_e dependence has been observed for F_p, G_p, $\tilde{G}_p$ and H_p within the available statistics.

Bin number	$M_{\pi\pi}$ barycenter (MeV/c^2)	dimensionless form factors F_s	$\tilde{G}_p$
1	286.06	5.7195(3)(3)	4.334(74)(19)
2	295.95	5.8123(3)(1)	4.422(53)(31)
3	304.88	5.8647(3)(2)	4.550(46)(25)
4	313.48	5.9134(3)(2)	4.645(41)(23)
5	322.02	5.9496(3)(1)	4.711(38)(28)
6	330.80	5.9769(3)(1)	4.767(35)(27)
7	340.17	6.0119(3)(1)	4.780(34)(30)
8	350.94	6.0354(3)(1)	4.907(34)(20)
9	364.57	6.0532(3)(1)	5.019(35)(19)
10	389.95	6.1314(3)(5)	5.163(36)(21)

Bin number	dimensionless form factors F_p	G_p	H_p
1	−0.181(67)(15)	5.053(258)(66)	−1.795(518)(193)
2	−0.324(62)(34)	5.186(142)(84)	−2.088(320)(77)
3	−0.209(60)(33)	4.941(108)(59)	−1.995(267)(98)
4	−0.156(58)(32)	4.896(91)(51)	−2.750(246)(72)
5	−0.366(55)(41)	5.245(80)(58)	−2.045(237)(98)
6	−0.383(54)(38)	5.283(73)(56)	−2.705(234)(88)
7	−0.218(55)(46)	5.054(68)(59)	−2.203(235)(156)
8	−0.302(54)(33)	5.264(62)(37)	−1.856(239)(110)
9	−0.309(54)(31)	5.357(57)(30)	−2.096(251)(217)
10	−0.264(59)(33)	5.418(55)(33)	−2.865(287)(177)

5 Summary

From a sample of 1.11×10^6 K_{e4} decay candidates with 0.95% background contamination, the branching fraction, inclusive of $K_{e4\gamma}$ decays, has been measured to be $\mathrm{BR}(K_{e4}) = (4.257 \pm 0.016_{\mathrm{exp}} \pm 0.031_{\mathrm{ext}}) \times 10^{-5}$ using $K_{3\pi}$ as normalization mode (the experimental error σ_{exp} is the quadratic sum of the statistical σ_{stat} and systematic σ_{syst} uncertainties). The relative 0.8% precision of the achieved measurement, dominated by the external uncertainty from the normalization mode, represents a factor of ~ 3 improvement with respect to the world average value, $\mathrm{BR}(K_{e4}) = (4.09 \pm 0.10) \times 10^{-5}$ based on two earlier measurements [17, 18]. The relative decay rate $\Gamma(K_{e4})/\Gamma(K_{3\pi}) = (7.615 \pm 0.030_{\mathrm{exp}}) \times 10^{-4}$ is measured with a 0.4% relative precision, a factor of ~ 5 improvement over the current world average value of $(7.31 \pm 0.16) \times 10^{-4}$.

The hadronic form factors that characterize the decay have been evaluated both for absolute value and energy dependence. The overall normalization form factor $F_s(q^2 = 0, S_e = 0)$ has been measured with a 0.6% total relative precision as $f_s = 5.705 \pm 0.017_{\mathrm{exp}} \pm 0.031_{\mathrm{ext}}$ when using values of kaon mean lifetime τ_K and $|V_{us}|$ from [10], a factor of ~ 2 and 4 improvement with respect to the values $f_s = 5.75 \pm 0.08$ [18] and $f_s = 5.59 \pm 0.14$ [17] obtained by earlier experiments. The achieved improved precision on K_{e4} rate and form factors brings new inputs to further theoretical studies and allows stronger tests of Chiral Perturbation Theory predictions.

Acknowledgments

We gratefully acknowledge the CERN SPS accelerator and beam line staff for the excellent performance of the beam and the technical staff of the participating institutes for their efforts in maintenance and operation of the detector. We enjoyed fruitful discussions about K_{e4} form factors theoretical descriptions with V. Bernard, G. Colangelo, S. Descotes-Genon, M. Knecht and P. Stoffer.

References

[1] T.D. Lee and C.S. Wu, Ann. Rev. Nucl. Sci. **16** (1966) 471.

[2] J.R. Batley *et al.*, Eur. Phys. J. **C70** (2010) 635.

[3] G. Colangelo, J. Gasser, H. Leutwyler, Phys. Lett. **B488** (2000) 261.

[4] G. Amoros, J. Bijnens, P. Talavera, Phys. Lett. **B480** (2000) 71.

[5] G. Amoros, J. Bijnens, P. Talavera, Nucl. Phys. **B602** (2001) 87.

[6] J. Bijnens, I. Jemos, Nucl. Phys. **B854** (2012) 631.

[7] J. Donoghue, J. Gasser, H. Leutwyler, Nucl. Phys. **B343** (1990) 341.

[8] J.R. Batley *et al.*, Eur. Phys. J. **C52** (2007) 875.

[9] V. Fanti *et al.*, Nucl. Inst. Methods **A574** (2007) 433.

[10] J. Beringer *et al.* (PDG), Phys. Rev. **D86** (2012) 010001.

[11] GEANT detector description and simulation tool, CERN program library long writeup W5013 (1994).

[12] J.R. Batley *et al.*, Phys. Lett. **B649** (2007) 349.

[13] E. Barberio and Z. Was, PHOTOS, Comp. Phys. Comm. **79** (1994) 291.

[14] Qingjun Xu and Z. Was, Proceedings of Science, PoS (RADCOR2009) (2009) 071, (http://pos.sissa.it/cgi-bin/reader/conf.cgi?confid=92).

[15] N. Cabibbo and A. Maksymowicz, Phys. Rev. **137** (1965) B438; Phys. Rev. **168** (1968) 1926.

[16] A. Pais and S. Treiman, Phys. Rev. **168** (1968) 1858.

[17] L. Rosselet *et al.*, Phys. Rev. **D15** (1977) 574.

[18] S. Pislak *et al.*, Phys. Rev. **D67** (2003) 072004.